

# Quantum Simulation of Dynamical Transition Rates in Open Quantum Systems

Robson Christie,<sup>1</sup> Kyunghyun Baek,<sup>2</sup> Jeongho Bang,<sup>2</sup> and Jaewoo Joo<sup>1</sup>

<sup>1</sup>School of Mathematics and Physics, University of Portsmouth, PO1 3FX, United Kingdom

<sup>2</sup>Institute for Convergence Research and Education in Advanced Technology,

Yonsei University, Seoul 03722, Republic of Korea

(Dated: September 12, 2025)

Estimating transition rates in open quantum systems is hampered by computing-resource demands that grow rapidly with system size. We present a quantum-simulation framework that enables efficient estimation by recasting the transition rate, given as the time derivative of an equilibrium correlation function, into a set of independently measurable contributions. Each contribution term is evaluated as the expectation value of a parameter-tuned quantum process, thereby circumventing explicit Lindbladian numerics. We validate our method on a spin- $\frac{1}{2}$  decoherence model using an IBM quantum processor. Further, we apply the method to the Caldeira–Leggett model of quantum Brownian motion as a realistic and practically relevant setting and reaffirm the theoretical soundness and practical implementability. These results provide evidence that quantum simulation can deliver substantial computational advantages in studying open-system kinetics on a quantum computer.

*Introduction*—Estimating transition rates are central to chemistry and statistical physics, underpinning barrier crossing, diffusion, and relaxation [1]. For metastable open systems governed by Markovian master equations, two dynamical objects suffice to characterize the rates: the equilibrium correlation  $C(t)$  and its time derivative  $\dot{C}(t)$ . In the flux-side correlation formalism, after a short intrabasin transient starting from  $A$  to  $B$ , the dynamics enter a linear-response window in which  $\dot{C}(t)$  approaches a plateau shown in Fig. 1. The interbasin rate  $k_{AB}$  is then read off as  $k_{AB} \simeq \dot{C}(t)$  for  $\tau_{\text{intra}} \ll t \ll \tau_{\text{eq}}$  before  $\dot{C}(t) \rightarrow 0$  at global equilibrium. Despite considerable advancements in classical numerics, estimating  $k_{AB}$  remains challenging: Lindblad propagation scales poorly with Hilbert-space dimension; plateau extraction from long-time correlators is sample-hungry; and structured environments introduce noise and memory effects [2, 3].

Quantum simulation has rapidly matured into a powerful tool for exploring quantum dynamics beyond state-of-the-art classical numerics, with notable demonstrations across quantum chemistry [4–8], many-body physics [9–11], quantum field theory [12–14], and cosmology [15–17]. In the near term, noisy intermediate-scale quantum (NISQ) devices motivate methods tailored to limited qubit counts, shallow depths, and hardware noise [18–20]. Simulation of open-system dynamics using quantum master-equation primitives particularly incorporates environmental effects through non-unitary channels, avoiding explicit bath simulation and improving scalability for complex open dynamics [21–27], with the potential to establish a quantum-enhanced toolkit for real-world applications [28].

Motivated by these challenges, we develop a hardware-ready framework that estimates transition rates by reducing the time derivative of the quantum time-correlation function to a finite set of independently measurable ex-

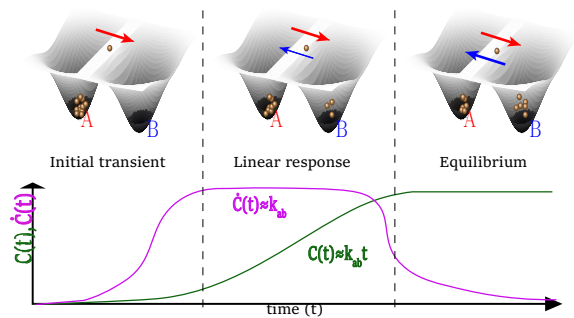


FIG. 1. Metastable-transition dynamics:  $C(t)$  (green) grows approximately linearly after an intrabasin transient, while the transition rate  $\dot{C}(t)$  (violet) exhibits a plateau  $\dot{C}(t) \approx k_{AB}$  for  $\tau_{\text{intra}} \ll t \ll \tau_{\text{eq}}$  before decaying to zero at equilibrium ( $\tau_{\text{intra}}$ : intrabasin relaxation time and  $\tau_{\text{eq}}$ : global equilibrium time).

pectation values such as

$$k_{AB} \approx \frac{\sum_j \langle \hat{O}_j \rangle_\Phi}{\langle \hat{O}^* \rangle}. \quad (1)$$

Each expectation contribution is obtained by executing a parameter-tuned completely positive trace-preserving process (CPTP)  $\Phi$  and measuring a single observable  $\hat{O}_j$  (with normalization by  $\langle \hat{O}^* \rangle$ ). This derivative-to-expectation reduction dispenses with explicit Lindbladian integration and long-time trajectory averaging: all quantities are single-time, shallow-depth, and parallel across terms. We validate the workflow on an IBM quantum processor using a spin-1/2 decoherence model and find close agreement with theory across a range of dissipation strengths. We then apply the scheme to the Caldeira–Leggett model of quantum Brownian motion [29, 30] where system-bath structure matters and demonstrate its stability and implementability over experimentally relevant parameter ranges. Taken together, these results introduce a distinct route to kinetics on quantum

hardware and indicate a credible path toward practical quantum advantages.

*Lindblad evolution*—The reduced dynamics of an open quantum system coupled to an environment are described by a CPTP map. When bath correlations decay on short timescales compared with the system’s evolution, the Markovian limit is realized. Then, the dynamical maps form a semigroup generated by the Lindblad master equation with its system  $\hat{\rho}_S$  [31–33]

$$\begin{aligned} \frac{d}{dt}\hat{\rho}_S &= \mathcal{L}(\hat{\rho}_S(t)) \\ &= -\frac{i}{\hbar}[\hat{H}, \hat{\rho}_S] + \frac{1}{\hbar} \sum_k \left( \hat{L}_k \hat{\rho}_S \hat{L}_k^\dagger - \frac{1}{2} \{ \hat{\rho}_S, \hat{L}_k^\dagger \hat{L}_k \} \right), \quad (2) \end{aligned}$$

where  $[., .]$  and  $\{., .\}$  denote the commutator and anticommutator,  $\hat{H}$  generates the unitary part, and the set of  $\hat{L}_k$  encodes environmental effects (rates absorbed into  $\hat{L}_k$ ). For instance, Hermitian  $\hat{L}_k$  describes pure dephasing, whereas non-Hermitian  $\hat{L}_k$  captures energy exchange such as dissipation and thermalization [34, 35].

*Quantum correlation functions*—To characterize transitions between coarse-grained regions  $A$  and  $B$  of phase space, we introduce the one-dimensional (1D) projectors

$$\hat{\theta}_A = \int_{x \in A} dx |x\rangle \langle x|, \quad \hat{\theta}_B = \int_{x \in B} dx |x\rangle \langle x|, \quad (3)$$

with position eigenstates  $|x\rangle$ . By  $\langle \hat{O} \rangle_{\text{eq}} \equiv \text{Tr}(\hat{\rho}_{\text{eq}} \hat{O})$  for the equilibrium average with  $\mathcal{L}(\hat{\rho}_{\text{eq}}) = 0$ , the normalized correlation and its time derivative are given by

$$\begin{aligned} C(t) &= \frac{\langle \{\hat{\theta}_A(0), \hat{\theta}_B(t)\} \rangle_{\text{eq}}}{2 \langle \hat{\theta}_A(0) \rangle_{\text{eq}}}, \\ \dot{C}(t) &= \frac{\langle \{\hat{\theta}_A(0), \dot{\hat{\theta}}_B(t)\} \rangle_{\text{eq}}}{2 \langle \hat{\theta}_A(0) \rangle_{\text{eq}}}, \quad (4) \end{aligned}$$

where  $\hat{\theta}_B(t) = e^{\mathcal{L}^\dagger t}(\hat{\theta}_B(0))$  and  $\dot{\hat{\theta}}_B(t) = \mathcal{L}^\dagger(\hat{\theta}_B(t))$  in the Heisenberg picture. Equivalently, in the Schrödinger picture, one evolves the state and keeps  $\hat{\theta}_B$  fixed as

$$\begin{aligned} C(t) &= \frac{\text{tr} \left( \hat{\theta}_B e^{\mathcal{L} t} (\{\hat{\rho}_{\text{eq}}, \hat{\theta}_A\}) \right)}{2 \langle \hat{\theta}_A \rangle_{\text{eq}}}, \\ \dot{C}(t) &= \frac{\text{tr} \left( \hat{\theta}_B \mathcal{L} \left( e^{\mathcal{L} t} (\{\hat{\rho}_{\text{eq}}, \hat{\theta}_A\}) \right) \right)}{2 \langle \hat{\theta}_A \rangle_{\text{eq}}}, \quad (5) \end{aligned}$$

where  $\hat{\theta}_{A/B}(0) \equiv \hat{\theta}_{A/B}$ . The detailed derivation of Eq. (5) is provided in the Supplementary Materials.

*Parameter-tunable quantum process*—We realize the reduction to single-time expectation values using a control qubit initialized in  $\hat{c}_+ = |+\rangle \langle +|$  for  $|+ \rangle = (|0\rangle + |1\rangle)/\sqrt{2}$  and two system registers shown in Fig. 2. The first register is prepared in the projector state  $\hat{\theta}_B$  (normally expressed by a mixed state), and the second in the

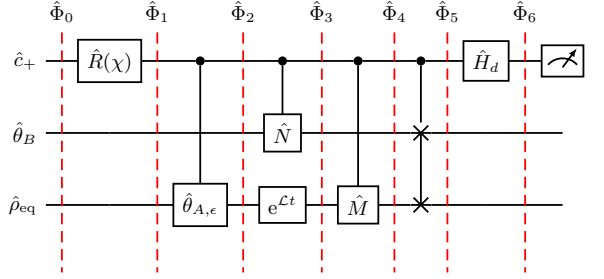


FIG. 2. Parameter-tunable quantum process for estimating  $C(t)$  and  $\dot{C}(t)$ . The control qubit is phase-shifted by  $\hat{R}(\chi)$  and read out after  $\hat{H}_d$ .  $\hat{\theta}_{A,\epsilon}$  is the small-angle surrogate in Eq. (10).  $e^{\mathcal{L} t}$  is the CW-Lindblad propagator, and  $\hat{N}$  and  $\hat{M}$  are Hamiltonian/jump/anticommutator channels. The states  $\hat{\Phi}$  in each step are given in the Supplementary Materials.

$\mathcal{E}$	$\mathcal{E}_{H1}$	$\mathcal{E}_{H2}$	$\mathcal{E}_J$	$\mathcal{E}_{AC1}$	$\mathcal{E}_{AC2}$
$\chi$	$-\frac{\pi}{2}$	$\frac{\pi}{2}$	0	0	0
$\hat{N}$	$\hat{\mathbb{1}}$	$\hat{H}$	$\hat{L}_k^\dagger$	$\hat{\mathbb{1}}$	$\hat{L}_k^\dagger \hat{L}_k$
$\hat{M}$	$\hat{H}$	$\hat{\mathbb{1}}$	$\hat{L}_k$	$\hat{L}_k$	$\hat{\mathbb{1}}$

TABLE I. Parameter settings for Fig. 2. Each row yields one expectation value  $\mathcal{E} = \langle \hat{\sigma}_z^c \rangle$  given in Eq. (7).

equilibrium state  $\hat{\rho}_{\text{eq}}$  with  $\mathcal{L}(\hat{\rho}_{\text{eq}}) = 0$ . On the control qubit, we apply a phase gate  $\hat{R}(\chi)$ , and we conditionally enact  $\hat{\theta}_{A,\epsilon}$ ,  $\hat{N}$ ,  $\hat{M}$ , and a controlled-SWAP gate between the two registers ( $\epsilon$ : angle parameter in a projector form). The open-system evolution block  $e^{\mathcal{L} t}$  is implemented via the repeated-interaction Cleve–Wang (CW) scheme [26], but can be replaced by sparse product formulas [36] or amplitude-amplified constructions [37]. After a Hadamard gate  $\hat{H}_d$ , measuring the control qubit in the  $Z$ -basis yields the scalar

$$\mathcal{E}(\chi; \hat{N}, \hat{M}; t, \epsilon) = \langle \hat{\sigma}_z^c \rangle, \quad (6)$$

from which contribution terms for  $C(t)$  and  $\dot{C}(t)$  are assembled (Pauli matrices:  $\hat{\sigma}_{x,y,z}$ ).

*Linear-combination estimator*—From the set of single-time expectation values, we obtain

$$\begin{aligned} C(t) &= \frac{\mathcal{E}_C}{2 \mathcal{E}_D}, \\ \dot{C}(t) &= \frac{\mathcal{E}_{H1} + \mathcal{E}_{H2} + \mathcal{E}_J + \mathcal{E}_{AC1} + \mathcal{E}_{AC2}}{2 \mathcal{E}_D}, \quad (7) \end{aligned}$$

where it shows  $\mathcal{E}_{H1/H2}$  for Hamiltonian parts,  $\mathcal{E}_J$  for the jump term,  $\mathcal{E}_{AC1/2}$  for the anticommutator contributions in Eq. (2). In addition, for  $\chi = 0$ ,  $\mathcal{E}_C$  and  $\mathcal{E}_D$  are given by  $\hat{N} = \hat{M} = \hat{\mathbb{1}}$  and  $\hat{\theta}_B = \hat{N} = \hat{M} = e^{\mathcal{L} t} = \hat{\mathbb{1}}$ , respectively. Each  $\mathcal{E}$  is obtained from a *single* circuitry configuration, which implies that no explicit Lindbladian integrals, long-time fits, or two-time correlator reconstructions are required.

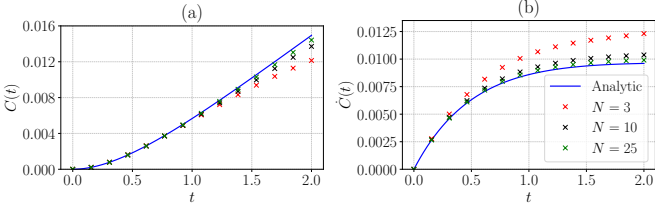


FIG. 3. Spin- $\frac{1}{2}$  testbed. (a)  $C(t)$  and (b)  $\dot{C}(t)$  versus  $t$  for  $\mu = 0.1$ ,  $\gamma_0 = 1$ ,  $\hbar = 1$ : analytics (blue, solid) vs CW-Lindblad emulation at  $N = 3, 10$ , and  $25$  time steps.

When  $\hat{N}$  or  $\hat{M}$  are Hermitian but not unitary, we implement them through the small-angle unitary surrogate

$$\hat{\mathcal{O}}_\epsilon = \frac{e^{i\epsilon\hat{\mathcal{O}}} - e^{-i\epsilon\hat{\mathcal{O}}}}{2i\epsilon}, \quad (8)$$

whose expectation value admits the rapidly convergent expansion

$$\langle \hat{\mathcal{O}}_\epsilon \rangle_\rho = \langle \hat{\mathcal{O}} \rangle_\rho - \frac{\epsilon^2}{3!} \langle \hat{\mathcal{O}}^3 \rangle_\rho + \frac{\epsilon^4}{5!} \langle \hat{\mathcal{O}}^5 \rangle_\rho - \dots, \quad (9)$$

and equals  $\langle \hat{\mathcal{O}} \rangle_\rho$  to leading order. Applying the same construction to the projector  $\hat{\theta}_A$  particularly yields

$$\hat{\theta}_{A,\epsilon} = \frac{\sin \epsilon}{\epsilon} \hat{\theta}_A, \quad (10)$$

for  $(\hat{\theta}_A)^2 = \hat{\theta}_A$ . This prefactor contribution is cancelled between its numerator and denominator in Eq. (5), so both  $C(t)$  and  $\dot{C}(t)$  become independent of  $\epsilon$  for  $\hat{\theta}_A$ .

*Motivative example: Spin- $\frac{1}{2}$  model*—We benchmark the estimator on an analytically solvable spin- $\frac{1}{2}$  system driven by a transverse field and continuously monitored in  $|0\rangle$  and  $|1\rangle$ . Then, the Lindblad generator comprises  $\hat{H} = \mu\hat{\sigma}_y$  and  $\hat{L} = \sqrt{\gamma_0}\hat{\sigma}_z$ . In the dephasing-dominated regime  $\mu \ll \gamma_0$ , the pointer states  $|0\rangle$  and  $|1\rangle$  are metastable ( $\gamma_0$ : decoherence rate). Choosing  $\hat{\theta}_A = |0\rangle\langle 0|$  and  $\hat{\theta}_B = |1\rangle\langle 1|$ , the stationary state is known as  $\hat{\rho}_{\text{eq}} = \frac{1}{2}(|0\rangle\langle 0| + |1\rangle\langle 1|)$ . Thus, the quantum correlation and its derivative admit closed forms

$$\begin{aligned} C(t) &= \frac{1}{2} \left[ 1 - e^{-\gamma_0 t / \hbar} \left( \cosh \omega t + \frac{\gamma_0}{\hbar \omega} \sinh \omega t \right) \right], \\ \dot{C}(t) &= \frac{2\mu^2}{\hbar^2 \omega} e^{-\gamma_0 t / \hbar} \sinh \omega t, \end{aligned} \quad (11)$$

with  $\omega = \sqrt{\gamma_0^2 - 4\mu^2}/\hbar$ . For example,  $\dot{C}(2.34) \approx 0.0096$  as a maximum value for  $\mu = 0.1$ ,  $\gamma_0 = 1$ ,  $\hbar = 1$ .

In Fig. 3, numerical QuTiP emulations of our method using the circuitry are compared with analytical results  $\mu = 0.1$ ,  $\gamma_0 = 1$ ,  $\hbar = 1$  in Eq. (11) [38]. Each emulation runs for  $N = 3, 10, 25$  time steps, recycling a single ancillary qubit inside the CW-Lindblad time evolution  $e^{\mathcal{L}t}$ . The discrepancy decreases systematically with finer time discretization since larger  $N$  implies shorter time step  $\delta = t/N$  in  $e^{\mathcal{L}t}$  (details in the Supplementary Materials).

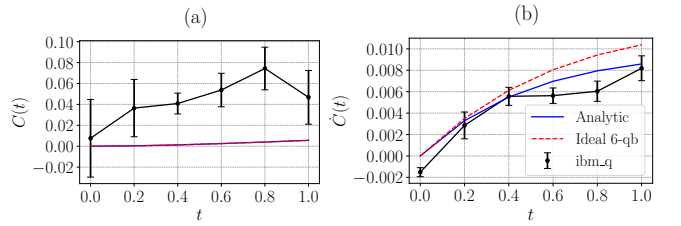


FIG. 4. IBM quantum hardware (six-qubit realization). (a)  $C(t)$  from ten batches of 20,000 shots and (b)  $\dot{C}(t)$  from five batches of 20,000 shots. Both are compared with analytics (blue, solid) and ideal six-qubit simulation (red, dashed) at  $t = \{0, 0.2, 0.4, 0.6, 0.8, 1.0\}$ .

For hardware validation, we execute the quantum simulation on IBMQ using six qubits: three main qubits for control,  $\hat{\theta}_B$ , and system initialized to  $\hat{\rho}_{\text{eq}}$ , and three ancillas for realizing  $N = 3$  repeated-interaction steps for  $e^{\mathcal{L}t}$ . For a minimal implementation, the controlled- $\hat{\theta}_A$  gate is decomposed using  $\hat{\theta}_A = |0\rangle\langle 0| = (\mathbb{1} + \hat{\sigma}_z)/2$ , reducing the primitive to a controlled- $\hat{\sigma}_z$  gate plus an identity branch. Further technical details and experimental data are provided in the Supplementary Materials.

We first estimate  $C(t)$  from ten independent batches of 20,000 shots at  $t = \{0, 0.2, 0.4, 0.6, 0.8, 1.0\}$  in Fig. 4 (a). The estimated  $C(t)$  increases with  $t$  and lies above ideal references. Note that the normalization  $\mathcal{E}_D = \text{tr}(\hat{\rho}_{\text{eq}}\hat{\theta}_A) = 1/2$  is set for this case. Fig. 4(b) shows the data of  $\dot{C}(t)$  from five batches of 20,000 shots and compares them with Eq. (11) and an ideal six-qubit simulation in Qiskit. Apart from a small offset at  $t = 0$ , which is due to the pure gate errors without time evolution, the experimental curve tracks the predicted shape closely. Interestingly, applying a uniform vertical shift yields excellent agreement with only minor residuals (no error-mitigation applied). Notably,  $\dot{C}(t)$  exhibits smaller standard errors than  $C(t)$  despite using half as many shots, consistent with

$$\dot{C}(t) = 2\mathcal{E}_{H1} = 2\mu\mathcal{E}_{\tilde{H}1}, \quad \tilde{H} = \hat{\sigma}_y, \quad (12)$$

which suppresses variance by the small coupling factor  $\mu^2 = 0.01$  ( $\tilde{H}$ : rescaled Hamiltonian without  $\mu$ ). Note that the cancellation of some expectation values arises in Eq. (12) due to the compensation of the jump and non-Hermitian terms each other, and numerical shot-noise tests in Qiskit corroborate that both  $C(t)$  and  $\dot{C}(t)$  converge toward ideal curves as the shot count increases (see the details in the Supplementary Materials).

*A realistic benchmark: Caldeira–Leggett double well*—We next study quantum Brownian motion in a 1D double well known as the Caldeira–Leggett model [29], where activated transport and slow relaxation are crucial and classical schemes can be costly with its system size. In the high-temperature limit (e.g.,  $k_B T$  well above the ground-state scale), the dynamics are captured by a

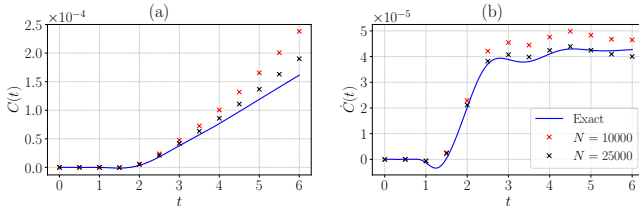


FIG. 5. Caldeira–Leggett double well: (a)  $C(t)$  and (b)  $\dot{C}(t)$  for  $m = 1$ ,  $k_B T = 0.0162$ ,  $\epsilon = 0.001$ ,  $\hbar = 0.01$ . Blue solid: direct numerics; markers: QuTiP emulation of Fig. 2 at  $N = 10^4$  and  $2.5 \times 10^4$  steps.

positivity-preserving Lindblad equation [34] with

$$\begin{aligned}\hat{H} &= \frac{\hat{P}^2}{2m} + \hat{V}(\hat{X}) + \frac{\gamma}{2} \left( \hat{X}\hat{P} + \hat{P}\hat{X} \right), \\ \hat{L} &= \sqrt{\gamma} \left( \lambda_T^{-1} \hat{X} + i\lambda_T \hat{P} \right),\end{aligned}\quad (13)$$

where  $\lambda_T = \sqrt{\hbar/(4mk_B T)}$  ( $k_B$ : Boltzmann constant).

The non-unitary observables  $\hat{X}$  and  $\hat{P}$  are implemented via the small-angle approximation with  $\epsilon$  in Eq. (8), with accuracy quantified in the Supplementary Materials. We discretize  $x \in [0, 1 - 2^{-n}]$  onto  $n$  grid qubits ( $\delta x = 2^{-n}$ ) and encode  $\hat{\rho}_{\text{eq}}$  and  $\hat{\theta}_{A/B}$  on the register. The projectors are prepared as normalized mixed states,

$$\begin{aligned}\hat{\rho}_A &= \mathcal{N}_A \hat{\theta}_A = \mathcal{N}_A \sum_{0.125 \leq x_k \leq 0.25} |x_k\rangle \langle x_k|, \\ \hat{\rho}_B &= \mathcal{N}_B \hat{\theta}_B = \mathcal{N}_B \sum_{0.75 \leq x_k \leq 0.875} |x_k\rangle \langle x_k|,\end{aligned}\quad (14)$$

where  $x_k$  is the  $k$ th grid point and  $\mathcal{N}_{A/B}$  are pre-known normalization factors from the projector sizes. The double-well potential is diagonal in the grid basis,

$$\hat{V}(\hat{X}) = 20 \sum_k (x_k - 0.2)^2 (x_k - 0.8)^2 |x_k\rangle \langle x_k|, \quad (15)$$

yielding a barrier  $V_B = 0.162$  in the double well. Note that we set  $k_B T = 0.1 V_B$  to probe activated dynamics without fully suppressing tunneling.

To initialize  $\hat{\rho}_{\text{eq}}$ , we can in general consider the propagation of an arbitrary state under  $\mathcal{L}$  until convergence to the fixed point  $\mathcal{L}(\hat{\rho}_{\text{eq}}) = 0$ . When  $\hat{\rho}_{\text{eq}}$  is Gibbsian like in the Caldeira–Leggett model, dedicated Gibbs-state sampler schemes can offer improved asymptotic scaling at the cost of additional preparation [39–41].

In Fig. 5, 11-qubit QuTip emulations use  $n = 5$  grid qubits (32 grid points) duplicated for  $\hat{\theta}_B$  and  $\hat{\rho}_{\text{eq}}$  plus a control qubit and the CW-Lindblad block uses  $N = 10^4$  and  $2.5 \times 10^4$  steps for the long-time evolution. Our method clearly reproduces both two important features such as short-time intrawell relaxation ( $1 \lesssim t \lesssim 2$ ) and the long-time plateau near  $t \approx 3$ . Increasing  $N$  again reduces time discretization error during  $e^{\mathcal{L}t}$ . Crucially, unlike direct long-time fits or full Liouville-space propagation,

our workflow assembles  $\dot{C}(t)$  from a constant number of single-time expectations.

*Discussion and outlook*—We introduced and demonstrated a hardware-ready framework for estimating transition rates in open quantum systems by reducing the time derivative of an equilibrium correlation function to a finite sum of single-time expectation values. This derivative-to-expectation reduction removes two bottlenecks: explicit Liouville-space propagation and long-time decay fitting. All required quantities are obtained from a constant number of independently executable circuit instances, compatible with shallow-depth NISQ devices. Our scheme was validated with two critical examples. First, the six-qubit IBMQ realization (spin-1/2 dephasing model) reproduced the analytical rate profile, establishing experimental viability of the estimator on contemporary quantum hardware. Second, the 11-qubit Caldeira–Leggett benchmark evidently captured both intrawell relaxation and the late-time plateau.

We would like to emphasize that a key advantage is resource scaling for real-world problems. For example, a 3D Caldeira–Leggett system discretized on a  $128^3$  grid needs  $2^{21}$  points and a dense classical density operator requires  $\sim (2^{21})^2$  complex entries at a fixed time, already at TiB-scale memory, while manipulating the superoperator is prohibitive even with sparsity. By contrast, our circuitry needs only  $2n + 1$  qubits to obtain  $C(t)$  or  $\dot{C}(t)$ , where  $n = \log_2(128^3) = 21$  qubits encode the grid, and 43 qubits (two registers for  $\hat{\theta}_B$  and  $\hat{\rho}_{\text{eq}}$  plus one control qubit) are required in total with  $\mathcal{O}(1)$  recyclable ancillas for the CW-Lindblad time evolution.

Furthermore, three developments will potentially strengthen applicability: (i) more faithful processors (e.g., mid-scale qubits, higher gate fidelities, error-mitigation); (ii) algorithmic upgrades for a new modular block  $e^{\mathcal{L}t}$  (e.g., sparse product-formula or amplitude-amplified Lindbladian simulation) to lower depth at fixed accuracy; and (iii) broader dynamical regimes via embeddings or auxiliary channels for non-Markovian settings. These could shift the model complexity into hardware-native primitives in the near future.

*Acknowledgments*—We acknowledge support from the Institute for Information & Communications Technology Promotion (IITP) grant funded by the Korea government (MSIP) (No. 2019-000003). J. B. and K. B. are supported by the Ministry of Trade, Industry, and Energy (MOTIE), Korea, under the project “Industrial Technology Infrastructure Program” (RS-2024-00466693) and by the National Research Foundation of Korea (NRF-2023M3K5A1094813 and RS-2023-00281456). This work is also supported by Grant No. K25L5M2C2 at the Korea Institute of Science and Technology Information (KISTI). We acknowledge utilization of IBM quantum services. The views expressed are those of the authors and do not reflect the official policy or position of IBM or the IBM Quantum team.

*Data Availability*—The data supporting this study are presented in the article and the Supplementary Materials, and are available from the corresponding authors upon reasonable request.

- 
- [1] M. A. Schlosshauer, *Decoherence: and the Quantum-to-Classical Transition* (Springer, Heidelberg, 2007).
- [2] C. Hsieh and R. Kapral, Entropy **16**, 200 (2013).
- [3] T. J. H. Hele, Mol. Phys. **115**, 1435 (2017).
- [4] S. McArdle *et al.*, Rev. Mod. Phys. **92**, 015003 (2020).
- [5] S. Guo *et al.*, Nat. Phys. **20**, 1 (2024).
- [6] H. H. S. Chan *et al.*, Sci. Adv. **9**, eab07484 (2023).
- [7] Y. Su *et al.*, PRX Quantum **2**, 040332 (2021).
- [8] B. Bauer *et al.*, Chem. Rev. **120**, 12685 (2020).
- [9] J. H. Busnaina *et al.*, Nat. Commun. **15**, 3065 (2024).
- [10] E. Chertkov *et al.*, Nat. Phys. **19**, 1799 (2023).
- [11] M. Cygorek *et al.*, Nat. Phys. **18**, 662 (2022).
- [12] B. Bauer *et al.*, PRX Quantum **4**, 027001 (2023).
- [13] Z. Davoudi, N. M. Linke, and G. Pagano, Phys. Rev. Res. **3**, 043072 (2021).
- [14] F. Schäfer *et al.*, Nat. Rev. Phys. **2**, 411 (2020).
- [15] S. Antonini and B. Swingle, Nat. Phys. **16**, 881 (2020).
- [16] J. Barata and S. Mukherjee, Phys. Rev. D **111**, L031901 (2025).
- [17] C. Viermann *et al.*, Nature **611**, 260 (2022).
- [18] J. Preskill, Quantum **2**, 79 (2018).
- [19] F. Arute *et al.*, Nature **574**, 505 (2019).
- [20] S. Chen *et al.*, Nat. Comm. **14**, 6001 (2023).
- [21] G. O. Samach *et al.*, Phys. Rev. Appl. **18**, 064056 (2022).
- [22] I. J. David, I. Sinayskiy, and F. Petruccione, Quanta **12**, 131 (2023).
- [23] S. Lee *et al.*, Nat. Comm. **14**, 1952 (2023).
- [24] H. Liu *et al.*, Quantum **9**, 1765 (2025).
- [25] J. D. Guimaraes *et al.*, Phys. Rev. A **109**, 052224 (2024).
- [26] R. Cleve and C. Wang, *the 44th International Colloquium on Automata, Languages, and Programming (ICALP 2017)* (Schloss Dagstuhl–Leibniz-Zentrum für Informatik, 2017) p. 17.
- [27] J. Joo and T. P. Spiller, New J. Phys. **25**, 083041 (2023).
- [28] F. Campaioli, J. H. Cole, and H. Hapuarachchi, PRX Quantum **5**, 020202 (2024).
- [29] A. O. Caldeira and A. J. Leggett, Phys. A: Stat. Mech. Appl. **121**, 587 (1983).
- [30] H. Breuer and F. Petruccione, *The Theory of Open Quantum Systems* (Oxford University Press, Oxford, 2002).
- [31] V. Gorini, A. Kossakowski, and E. C. G. Sudarshan, J. Math. Phys. **17**, 821 (1976).
- [32] G. Lindblad, Commun. Math. Phys. **48**, 119 (1976).
- [33] G. McCauley *et al.*, NPJ Quantum Inf. **6**, 74 (2020).
- [34] I. J. David, I. Sinayskiy, and F. Petruccione, Quanta **12**, 131 (2023).
- [35] D. Manzano, AIP Adv. **10**, 025106 (2020).
- [36] A. M. Childs and T. Li, Quantum Inf. Comput. **17**, 901 (2017).
- [37] X. Li and C. Wang, *the 50th International Colloquium on Automata, Languages, and Programming (ICALP 2023)* (Schloss Dagstuhl–Leibniz-Zentrum für Informatik, 2023) p. 87.
- [38] J. R. Johansson, P. D. Nation, and F. Nori, Comput. Phys. Commun. **183**, 1760 (2012).
- [39] M. Yung and A. Aspuru-Guzik, Proc. Natl. Acad. Sci. U.S.A. **109**, 754 (2012).
- [40] M. Motta *et al.*, Nat. Phys. **16**, 205 (2020).
- [41] P. Rall, C. Wang, and P. Wocjan, Quantum **7**, 1132 (2023).

## SUPPLEMENTARY MATERIALS

### Transition rate theory

We first review the classical transition rate theory based on [1], before introducing an analogous quantum formulation in Lindblad dynamics. To define a transition between the “states”, we first identify metastable subspaces  $A$  and  $B$  within the phase space of the system. We use characteristic functions to define the state functions for regions  $A$  and  $B$  as follows:

$$\theta_A(x) = \begin{cases} 1, & \text{if } x \in A, \\ 0, & \text{if } x \notin A, \end{cases} \quad \text{and} \quad \theta_B(x) = \begin{cases} 1, & \text{if } x \in B, \\ 0, & \text{if } x \notin B. \end{cases} \quad (16)$$

If we consider the case of many non-interacting particles at equilibrium, the populations of states  $A$  and  $B$  fluctuate due to transitions between these states. Consequently, the transition dynamics can be described by the temporal correlation of the states populations from point  $x_0$  to point  $x_t$  as follows:

$$C(t) = \frac{\langle \theta_A(x_0, 0) \theta_B(x_t, t) \rangle_{eq}}{\langle \theta_A(x_0, 0) \rangle_{eq}} \quad (17)$$

In this expression,  $\langle \cdot \rangle_{eq}$  represents the average over the equilibrium distribution of the initial state.

The correlation function  $C(t)$  is defined as the conditional probability of observing the system in state  $B$  at time  $t$  assuming that it started from state  $A$  at  $t = 0$  as shown in Fig. 1 in the main text. As described by linear response theory [1–3], the rate of equilibrium fluctuations from  $A$  to  $B$  is equal to the rate of relaxation as the system recovers from a non-equilibrium condition in which only state  $A$  is initially occupied. For brief intervals,  $C(t)$  reflects microscopic movements within state  $A$  and the transition state area, linked on the molecular time scale  $t_{mol}$  [1], which represents the time required to traverse the barrier separating the stable regions and settle into one of the states. However, on timescales longer than  $t_{mol}$ , a two-state kinetic model provides a good description of the transition dynamics. In this model, transitions are rare compared to the time spent in metastable states. The dynamical model can be represented as follows:

$$\frac{d}{dt} \langle \theta_A(t) \rangle_{ne} = -k_{AB} \langle \theta_A(t) \rangle_{ne} + k_{BA} \langle \theta_B(t) \rangle_{ne}, \quad (18)$$

$$\frac{d}{dt} \langle \theta_B(t) \rangle_{ne} = k_{AB} \langle \theta_A(t) \rangle_{ne} - k_{BA} \langle \theta_B(t) \rangle_{ne}. \quad (19)$$

The expectation values are taken with respect to time-dependent non-equilibrium phase-space probability densities, the solutions are

$$\langle \theta_A(t) \rangle_{ne} = \frac{k_{BA} + k_{AB} e^{-(k_{AB} + k_{BA})t}}{k_{AB} + k_{BA}}, \quad (20)$$

$$\langle \theta_B(t) \rangle_{ne} = \frac{k_{AB} (1 - e^{-(k_{AB} + k_{BA})t})}{k_{AB} + k_{BA}}, \quad (21)$$

which satisfy the kinetic equations with the initial conditions at  $t = 0$

$$\langle \theta_A(0) \rangle_{ne} = 1 \quad \text{and} \quad \langle \theta_B(0) \rangle_{ne} = 0. \quad (22)$$

After an initial transient time  $t_{mol}$ , the population dynamics of the double well system are well described by a two-state kinetic model. The initial conditions are equivalent to the definition of  $C(t)$  as the conditional probability of observing the system in state  $B$  at time  $t$  such that

$$C(t) = \langle \theta_B(t) \rangle_{ne}. \quad (23)$$

Expanding Eq. (21) for short times (first order in  $t$ ) in the linear response domain, the correlation function is

$$C(t) \approx k_{AB} t. \quad (24)$$

Therefore, if we start the system in the state  $A$ , the gradient of  $C(t)$  gives the rate constant  $\dot{C}(t) \approx k_{AB}$ .

The classical rate theory extends to quantum systems by replacing the classical characteristic functions with analogous projection operators:

$$\hat{\theta}_A = \int_{x \in A} dx |x\rangle \langle x| \quad \text{and} \quad \hat{\theta}_B = \int_{x \in B} dx |x\rangle \langle x|, \quad (25)$$

The quantum correlation function derivative is thus given by

$$\dot{C}_C(t) \equiv \frac{\langle \hat{\theta}_A(0) \dot{\hat{\theta}}_B(t) \rangle_{eq}}{\langle \hat{\theta}_A(0) \rangle_{eq}}. \quad (26)$$

and is complex-valued. The real part of Eq. (26) is identified as the rate, while the imaginary component contains phase information [4]. Since the projectors are Hermitian, the rate component of the correlation function is given by the anti-commutator expectation value

$$\dot{C}(t) \equiv \frac{\langle \{\hat{\theta}_A(0), \dot{\hat{\theta}}_B(t)\} \rangle_{eq}}{2 \langle \hat{\theta}_A(0) \rangle_{eq}}. \quad (27)$$

More explicitly, the above expression may be written with  $\hat{\theta}_{A/B}(0) \equiv \hat{\theta}_{A/B}$  in the form

$$\dot{C}(t) = \frac{\text{Tr}(\hat{\rho}_{eq} \left\{ \hat{\theta}_A, \mathcal{L}^\dagger(e^{\mathcal{L}^\dagger t}(\hat{\theta}_B)) \right\})}{2 \text{Tr}(\hat{\rho}_{eq} \hat{\theta}_A)}. \quad (28)$$

where  $\hat{\rho}_{eq}$  is the equilibrium state of the Lindblad dynamics and the time evolution of the observables is governed by the Heisenberg picture Lindblad evolution equation:

$$\begin{aligned} \frac{d}{dt} \hat{\theta}(t) &= \mathcal{L}^\dagger(\hat{\theta}(t)) = \frac{i}{\hbar} [\hat{H}, \hat{\theta}(t)] + \\ &\quad \frac{1}{\hbar} \sum_k \left( \hat{L}_k^\dagger \hat{\theta}(t) \hat{L}_k - \frac{1}{2} \{ \hat{\theta}(t), \hat{L}_k^\dagger \hat{L}_k \} \right). \end{aligned} \quad (29)$$

By expanding the commutators and rearranging the terms in Eq. (28), we can reformulate  $C(t)$  and  $\dot{C}(t)$  in terms of the Schrödinger picture dynamics as follows

$$C(t) = \frac{\text{Tr}(\hat{\theta}_B(e^{\mathcal{L}t}(\{\hat{\rho}_{eq}, \hat{\theta}_A\})))}{2 \text{Tr}(\hat{\rho}_{eq}\hat{\theta}_A)} \quad (30)$$

$$\dot{C}(t) = \frac{\text{Tr}(\hat{\theta}_B \mathcal{L}(e^{\mathcal{L}t}(\{\hat{\rho}_{eq}, \hat{\theta}_A\})))}{2 \text{Tr}(\hat{\rho}_{eq}\hat{\theta}_A)}. \quad (31)$$

with the standard form of the Lindblad equation:

$$\begin{aligned} \frac{d}{dt}\hat{\rho}(t) &= \mathcal{L}(\hat{\rho}(t)) = -\frac{i}{\hbar}[\hat{H}, \hat{\rho}(t)] \\ &+ \frac{1}{\hbar} \sum_k \left( \hat{L}_k \hat{\rho}(t) \hat{L}_k^\dagger - \frac{1}{2} \{\hat{\rho}(t), \hat{L}_k^\dagger \hat{L}_k\} \right). \end{aligned} \quad (32)$$

### Correlation derivative circuit

Here we provide the mathematical details for the expectation value corresponding to a  $\hat{\sigma}_z$  measurement on the control qubit in the Schrödinger picture correlation derivative circuit given in Fig. 6(c)

$$\begin{aligned} \text{Tr}(\hat{\sigma}_z^c \hat{\Phi}_6) &= \frac{1}{2} \left( e^{-i\chi} \text{Tr}(\hat{\theta}_B \hat{N}^\dagger e^{\mathcal{L}t}(\hat{\rho}_{eq}\hat{\theta}_A) \hat{M}^\dagger) \right. \\ &\quad \left. + e^{i\chi} \text{Tr}(\hat{\theta}_B \hat{M} e^{\mathcal{L}t}(\hat{\theta}_A \hat{\rho}_{eq}) \hat{N}) \right), \end{aligned} \quad (33)$$

where the superscript c in  $\hat{\sigma}_z^c$  indicates the  $\hat{\sigma}_z$  Pauli operator on the control qubit. We denote the total density operator at stage  $n$  by  $\hat{\Phi}_n$ . Our initial circuit input is the state

$$\hat{\Phi}_0 = |+\rangle\langle+| \otimes \hat{\theta}_B \otimes \hat{\rho}_{eq}, \quad (34)$$

with the control qubit in the  $|+\rangle$  state, and the projection operator  $\hat{\theta}_B$  together with  $\hat{\rho}_{eq}$ . In the next stage, we apply a phase-shifted  $z$ -axis rotation operator to the control qubit, such as  $\hat{R}(\chi) = e^{-i\chi(\hat{\sigma}_z - 1)/2}$ . The state  $\hat{\Phi}_1$  is given by

$$\hat{\Phi}_1 = \frac{1}{2} (|0\rangle\langle 0| + e^{-i\chi}|0\rangle\langle 1| + e^{i\chi}|1\rangle\langle 0| + |1\rangle\langle 1|) \otimes \hat{\theta}_B \otimes \hat{\rho}_{eq}. \quad (35)$$

After the controlled- $\hat{\theta}_A$  gate as in Fig. 6,  $\hat{\Phi}_2$  is given by

$$\begin{aligned} \hat{\Phi}_2 &= \frac{1}{2} (|0\rangle\langle 0| \otimes \hat{\theta}_B \otimes \hat{\rho}_{eq} + e^{-i\chi}|0\rangle\langle 1| \otimes \hat{\theta}_B \otimes \hat{\rho}_{eq}\hat{\theta}_A \\ &+ e^{i\chi}|1\rangle\langle 0| \otimes \hat{\theta}_B \otimes \hat{\theta}_A \hat{\rho}_{eq} + |1\rangle\langle 1| \otimes \hat{\theta}_B \otimes \hat{\theta}_A \hat{\rho}_{eq}\hat{\theta}_A). \end{aligned} \quad (36)$$

Applying the controlled- $\hat{N}$  gate and the Lindblad time evolution gate  $e^{\mathcal{L}t}$  [5] in Fig. 6 results in

$$\begin{aligned} \hat{\Phi}_3 &= \frac{1}{2} \left( |0\rangle\langle 0| \otimes \hat{\theta}_B \otimes \hat{\rho}_{eq} \right. \\ &+ e^{-i\chi}|0\rangle\langle 1| \otimes \hat{\theta}_B \hat{N}^\dagger \otimes e^{\mathcal{L}t}(\hat{\rho}_{eq}\hat{\theta}_A) \\ &+ e^{i\chi}|1\rangle\langle 0| \otimes \hat{N}\hat{\theta}_B \otimes e^{\mathcal{L}t}(\hat{\theta}_A \hat{\rho}_{eq}) \\ &\left. + |1\rangle\langle 1| \otimes \hat{N}\hat{\theta}_B \hat{N}^\dagger \otimes \hat{e}^{\mathcal{L}t}(\hat{\theta}_A \hat{\rho}_{eq}\hat{\theta}_A) \right). \end{aligned} \quad (37)$$

Subsequently, applying the controlled- $\hat{M}$  gate in Fig. 6 yields

$$\begin{aligned} \hat{\Phi}_4 &= \frac{1}{2} \left( |0\rangle\langle 0| \otimes \hat{\theta}_B \otimes \hat{\rho}_{eq} \right. \\ &+ e^{-i\chi}|0\rangle\langle 1| \otimes \hat{\theta}_B \hat{N}^\dagger \otimes e^{\mathcal{L}t}(\hat{\rho}_{eq}\hat{\theta}_A) \hat{M}^\dagger \\ &+ e^{i\chi}|1\rangle\langle 0| \otimes \hat{N}\hat{\theta}_B \otimes \hat{M} e^{\mathcal{L}t}(\hat{\theta}_A \hat{\rho}_{eq}) \\ &\left. + |1\rangle\langle 1| \otimes \hat{N}\hat{\theta}_B \hat{N}^\dagger \otimes \hat{M} e^{\mathcal{L}t}(\hat{\theta}_A \hat{\rho}_{eq}\hat{\theta}_A) \hat{M}^\dagger \right). \end{aligned} \quad (38)$$

After the block C-SWAP gates [6], the density operator becomes

$$\begin{aligned} \hat{\Phi}_5 &= \frac{1}{2} \left( |0\rangle\langle 0| \otimes \hat{\theta}_B \otimes \hat{\rho}_{eq} \right. \\ &+ e^{-i\chi}|0\rangle\langle 1| \otimes \hat{\theta}_B \hat{N}^\dagger \xrightarrow[b]{\otimes} e^{\mathcal{L}t}(\hat{\rho}_{eq}\hat{\theta}_A) \hat{M}^\dagger \\ &+ e^{i\chi}|1\rangle\langle 0| \otimes \hat{N}\hat{\theta}_B \xrightarrow[k]{\otimes} \hat{M} e^{\mathcal{L}t}(\hat{\theta}_A \hat{\rho}_{eq}) \\ &\left. + |1\rangle\langle 1| \otimes \hat{M} e^{\mathcal{L}t}(\hat{\theta}_A \hat{\rho}_{eq}\hat{\theta}_A) \hat{M}^\dagger \otimes \hat{N}\hat{\theta}_B \hat{N}^\dagger \right). \end{aligned} \quad (39)$$

We finally have the state after the Hadamard gate such as

$$\begin{aligned} \hat{\Phi}_6 &= \frac{1}{2} (|+\rangle\langle+| \otimes \hat{\theta}_B \otimes \hat{\rho}_{eq} \\ &+ e^{-i\chi}|+\rangle\langle-| \otimes \hat{\theta}_B \hat{N}^\dagger \xrightarrow[b]{\otimes} e^{\mathcal{L}t}(\hat{\rho}_{eq}\hat{\theta}_A) \hat{M}^\dagger \\ &+ e^{i\chi}|-\rangle\langle+| \otimes \hat{N}\hat{\theta}_B \xrightarrow[k]{\otimes} \hat{M} e^{\mathcal{L}t}(\hat{\theta}_A \hat{\rho}_{eq}) \\ &+ |-\rangle\langle-| \otimes \hat{M} e^{\mathcal{L}t}(\hat{\theta}_A \hat{\rho}_{eq}\hat{\theta}_A) \hat{M}^\dagger \otimes \hat{N}\hat{\theta}_B \hat{N}^\dagger). \end{aligned} \quad (40)$$

After performing the measurements in the control qubit, we have the expectation value

$$\begin{aligned} \text{Tr}(\hat{\sigma}_z^c \hat{\Phi}_6) &= \frac{1}{2} \left( e^{-i\chi} \text{Tr}(\hat{\theta}_B \hat{N}^\dagger e^{\mathcal{L}t}(\hat{\rho}_{eq}\hat{\theta}_A) \hat{M}^\dagger) \right. \\ &\quad \left. + e^{i\chi} \text{Tr}(\hat{\theta}_B \hat{M} e^{\mathcal{L}t}(\hat{\theta}_A \hat{\rho}_{eq}) \hat{N}) \right). \end{aligned} \quad (41)$$

In Fig. 2 in the main text we give a single circuit which can simulate the seven expectation values

$$C(t) = \frac{\mathcal{E}_C}{2\mathcal{E}_D}, \quad (42)$$

$$\dot{C}(t) = \frac{\mathcal{E}_{H1} + \mathcal{E}_{H2} + \mathcal{E}_J + \mathcal{E}_{AC1} + \mathcal{E}_{AC2}}{2\mathcal{E}_D}, \quad (43)$$

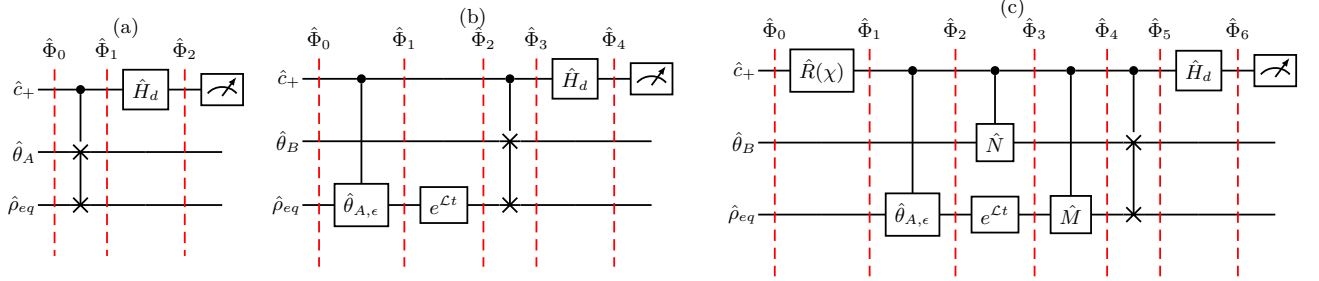


FIG. 6. Quantum circuits for evaluating (a)  $\mathcal{E}_D$ , (b)  $\mathcal{E}_C$ , and (c) the various terms of Eq. (43).

using the input combinations in Table 1 in the main text. In practice, using the same circuit for all seven expectation values is not the most efficient strategy, which is why we also give the equivalent (simpler) circuits in Fig. 6.

$\mathcal{E}_D$ —The denominator in Eqs. (43) and (42) can be calculated by the circuit in Fig. 6 (a), which is equivalent to Fig. 6 (c) without time evolution ( $\exp(\mathcal{L}t) = \hat{1}$ ) with  $\chi = 0$ ,  $\hat{N} = \hat{1}$ ,  $\hat{M} = \hat{1}$  and we enter  $\hat{\theta}_B = \hat{1}$ .

$$\mathcal{E}_D = \text{Tr}\left(\hat{\sigma}_z^c \hat{\Phi}_6\right) = \frac{1}{2} \left( \text{Tr}\left(\hat{\rho}_{eq} \hat{\theta}_A\right) + \text{Tr}\left(\hat{\theta}_A \hat{\rho}_{eq}\right) \right). \quad (44)$$

$\mathcal{E}_C$ —The correlation function numerator is calculated with Fig. 6 (b), or equivalently (c) with inputs  $\chi = 0$ ,  $\hat{N} = \hat{1}$ , and  $\hat{M} = \hat{1}$  to give

$$\mathcal{E}_C = \text{Tr}\left(\hat{\sigma}_z^c \hat{\Phi}_6\right) = \text{Tr}\left(\hat{\theta}_B \left(e^{\mathcal{L}t} \left(\{\hat{\rho}_{eq}, \hat{\theta}_A\}\right)\right)\right). \quad (45)$$

The correlation derivative numerator in Eq. (43) is given by the sum of five input combinations into the circuit in Fig. 6 (c) divided by  $2\mathcal{E}_D$  as shown in Eq. (43).  $\mathcal{E}_{H1}$  &  $\mathcal{E}_{H2}$ —For the Hamiltonian contributions, we first have  $\chi = -\pi/2$ ,  $\hat{N} = \hat{1}$ , and  $\hat{M} = \hat{H}$  and thus

$$\mathcal{E}_{H1} = \frac{1}{\hbar} \text{Tr}\left(\hat{\sigma}_z^c \hat{\Phi}_6\right) = \frac{1}{2\hbar} \left( i \text{Tr}\left(\hat{\theta}_B e^{\mathcal{L}t} \left(\hat{\rho}_{eq} \hat{\theta}_A\right) \hat{H}\right) - i \text{Tr}\left(\hat{\theta}_B \hat{H} e^{\mathcal{L}t} \left(\hat{\theta}_A \hat{\rho}_{eq}\right)\right) \right) \quad (46)$$

then we have  $\chi = \pi/2$ ,  $\hat{N} = \hat{H}$ , and  $\hat{M} = \hat{1}$

$$\mathcal{E}_{H2} = \frac{1}{\hbar} \text{Tr}\left(\hat{\sigma}_z^c \hat{\Phi}_6\right) = \frac{1}{2\hbar} \left( -i \text{Tr}\left(\hat{\theta}_B \hat{H} e^{\mathcal{L}t} \left(\hat{\rho}_{eq} \hat{\theta}_A\right)\right) + i \text{Tr}\left(\hat{\theta}_B e^{\mathcal{L}t} \left(\hat{\theta}_A \hat{\rho}_{eq} \hat{H}\right)\right) \right) \quad (47)$$

Combining Eq. (46) and Eq. (47) we have

$$\mathcal{E}_{H1} + \mathcal{E}_{H2} = -\frac{i}{2\hbar} \text{Tr}\left(\hat{\theta}_B \left[\hat{H}, e^{\mathcal{L}t} \left(\{\hat{\rho}_{eq}, \hat{\theta}_A\}\right)\right]\right). \quad (48)$$

$\mathcal{E}_J$ —For the jump term contribution we set  $\chi = 0$ ,  $\hat{N} = \hat{L}^\dagger$ , and  $\hat{M} = \hat{L}$

$$\mathcal{E}_J = \frac{1}{\hbar} \text{Tr}\left(\hat{\sigma}_z^c \hat{\Phi}_6\right) = \frac{1}{2\hbar} \left( \text{Tr}\left(\hat{\theta}_B \hat{L} e^{\mathcal{L}t} \left(\{\hat{\rho}_{eq}, \hat{\theta}_A\}\right) \hat{L}^\dagger\right) \right) \quad (49)$$

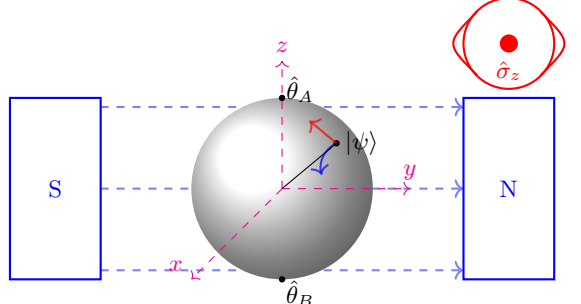


FIG. 7. Bloch sphere dynamics of a spin-1/2 system in Eq. (53), magnetic field rotates around  $y$ -axis while  $z$ -axis measurement drives the system towards the nearest pole. If  $\mu \ll \gamma$ , the system exhibits metastable transitions between the two poles ( $\hat{\theta}_A$  and  $\hat{\theta}_B$ ).

$\mathcal{E}_{NH1}$  &  $\mathcal{E}_{NH2}$ —The anti-commutator contribution consists of two measurements first  $\chi = 0$ ,  $\hat{N} = \hat{1}$  and  $\hat{M} = \hat{L}^\dagger \hat{L}$

$$\begin{aligned} \mathcal{E}_{AC1} &= -\frac{1}{2\hbar} \text{Tr}\left(\hat{\sigma}_z^c \hat{\Phi}_6\right) = \\ &- \frac{1}{4\hbar} \left( \text{Tr}\left(\hat{\theta}_B e^{\mathcal{L}t} \left(\hat{\rho}_{eq} \hat{\theta}_A\right) \hat{L}^\dagger \hat{L}\right) + \text{Tr}\left(\hat{\theta}_B \hat{L}^\dagger \hat{L} e^{\mathcal{L}t} \left(\hat{\theta}_A \hat{\rho}_{eq}\right)\right) \right) \end{aligned} \quad (50)$$

and next  $\chi = 0$ ,  $\hat{N} = \hat{L}^\dagger \hat{L}$  and  $\hat{M} = \hat{1}$

$$\begin{aligned} \mathcal{E}_{AC2} &= -\frac{1}{2\hbar} \text{Tr}\left(\hat{\sigma}_z^c \hat{\Phi}_6\right) = -\frac{1}{4\hbar} \left( \text{Tr}\left(\hat{\theta}_B \hat{L}^\dagger \hat{L} e^{\mathcal{L}t} \left(\hat{\rho}_{eq} \hat{\theta}_A\right)\right) \right. \\ &\quad \left. + \text{Tr}\left(\hat{\theta}_B e^{\mathcal{L}t} \left(\hat{\theta}_A \hat{\rho}_{eq}\right) \hat{L}^\dagger \hat{L}\right) \right) \end{aligned} \quad (51)$$

Combining Eq. (50) and Eq. (51) we have

$$\mathcal{E}_{AC1} + \mathcal{E}_{AC2} = -\frac{1}{4\hbar} \text{Tr}\left(\hat{\theta}_B \left\{ \hat{L}^\dagger \hat{L}, e^{\mathcal{L}t} \left(\{\hat{\rho}_{eq}, \hat{\theta}_A\}\right)\right\}\right) \quad (52)$$

Combining all these terms, we can evaluate the transition rate in Eq. (43).

### Decohering spin-1/2 transitions

A simple open quantum system to study the transition rate is a single spin-1/2 system with a magnetic field and continuous measurements, as shown in Fig. 7. The magnetic field along the  $y$ -axis causes the spin state to precess, whereas measurement in the  $z$ -direction localises the system at a pole, most likely the nearest one. This system is described by a Lindblad equation of the same form as Eq. (32) with Hamiltonian and Lindbladian operators.

$$\hat{H} = \mu\hat{\sigma}_y \quad \text{and} \quad \hat{L} = \sqrt{\gamma}\hat{\sigma}_z. \quad (53)$$

When  $\mu$  is significantly smaller than  $\gamma$ , this system exhibits metastable transitions between the two poles

$$\hat{\theta}_A = |0\rangle\langle 0| \quad \text{and} \quad \hat{\theta}_B = |1\rangle\langle 1|. \quad (54)$$

The stationary/equilibrium state of this system is the fully mixed state  $\hat{\rho}_{eq} = (|0\rangle\langle 0| + |1\rangle\langle 1|)/2$ . We can analytically solve these Lindblad dynamics for the correlation function and its rate expressions such as

$$C(t) = \frac{1}{2} \left( 1 - e^{-\frac{\gamma}{\hbar}t} \left( \cosh(\omega t) + \frac{\gamma}{\hbar\omega} \sinh(\omega t) \right) \right), \quad (55)$$

$$\dot{C}(t) = \frac{2\mu^2}{\hbar^2\omega} e^{-\frac{\gamma}{\hbar}t} \sinh(\omega t), \quad (56)$$

with  $\omega = \sqrt{(\gamma^2 - 4\mu^2)/\hbar^2}$ .

Table II presents the analytic expressions for all terms that contribute to the correlation function  $C(t)$ . Among all the contributions, the combinations  $\hat{\rho}_{eq} = |1\rangle\langle 1|$  with  $\hat{\theta}_A = \hat{1}$  and  $\hat{\rho}_{eq} = |1\rangle\langle 1|$  with  $\hat{\theta}_A = \hat{\sigma}_z$  exactly cancel each other out exactly. The remaining two combinations,  $\hat{\rho}_{eq} = |0\rangle\langle 0|$  with  $\hat{\theta}_A = \hat{1}$  and  $\hat{\rho}_{eq} = |0\rangle\langle 0|$  with  $\hat{\theta}_A = \hat{\sigma}_z$ , yield identical contributions. This allows us to perform one of the quantum circuits only with  $\hat{\rho}_{eq} = |0\rangle\langle 0|$  to compute the correlation function  $C(t)$ .

Table III gives analytic expressions for all terms contributing to the time derivative of the correlation function  $\dot{C}(t)$ . We observe cancellation between the jump and anti-commutator contributions, with the Hamiltonian parts  $\mathcal{E}_{H1}$  and  $\mathcal{E}_{H2}$  giving identical contributions that sum to give the rate (when divided by  $2\langle\hat{\theta}_A\rangle_{eq} = 1$ ). We can thus calculate the correlation derivative as

$$\dot{C}(t) = 2\mathcal{E}_{H1}(t), \quad (57)$$

for the spin-1/2 model.

### Experimental methods on the *ibm\_brisbane* device

Figs. 8 and 9 present the two circuits run on the *ibm\_brisbane* superconducting processor to obtain the correlation function  $C(t)$  and its time derivative  $\dot{C}(t)$ ,

$\hat{\rho}_{eq}$	$\hat{\theta}_A$	$\mathcal{E}$
$ 0\rangle\langle 0 $	$\hat{1}$	$\frac{1}{2} \left( 1 - e^{-\frac{\gamma}{\hbar}t} \left( \cosh(\omega t) + \frac{\gamma}{\hbar\omega} \sinh(\omega t) \right) \right)$
$ 0\rangle\langle 0 $	$\hat{\sigma}_z$	$\frac{1}{2} \left( 1 - e^{-\frac{\gamma}{\hbar}t} \left( \cosh(\omega t) + \frac{\gamma}{\hbar\omega} \sinh(\omega t) \right) \right)$
$ 1\rangle\langle 1 $	$\hat{1}$	$\frac{1}{2} \left( 1 + e^{-\frac{\gamma}{\hbar}t} \left( \cosh(\omega t) + \frac{\gamma}{\hbar\omega} \sinh(\omega t) \right) \right)$
$ 1\rangle\langle 1 $	$\hat{\sigma}_z$	$-\frac{1}{2} \left( 1 + e^{-\frac{\gamma}{\hbar}t} \left( \cosh(\omega t) + \frac{\gamma}{\hbar\omega} \sinh(\omega t) \right) \right)$

TABLE II. Analytic expectation value expressions contributing to the correlation function in Eq. (55) for the decohering spin-1/2 model with Eq. (53).

Term	$\chi$	$\hat{N}$	$\hat{M}$	$\hat{\theta}_A$	$\mathcal{E}$
$\mathcal{E}_{H1}$	$-\frac{\pi}{2}$	$\hat{1}$	$\hat{H} = \mu\hat{\sigma}_y$	$\hat{1}$ $\hat{\sigma}_z$	$0$ $\frac{\mu^2}{\hbar^2\omega} e^{-\frac{\gamma}{\hbar}t} \sinh(\omega t)$
$\mathcal{E}_{H2}$	$\frac{\pi}{2}$	$\hat{H} = \mu\hat{\sigma}_y$	$\hat{1}$	$\hat{1}$ $\hat{\sigma}_z$	$0$ $\frac{\mu^2}{\hbar^2\omega} e^{-\frac{\gamma}{\hbar}t} \sinh(\omega t)$
$\mathcal{E}_J$	0	$\hat{L}^\dagger = \sqrt{\gamma}\hat{\sigma}_z$	$\hat{L} = \sqrt{\gamma}\hat{\sigma}_z$	$\hat{1}$ $\hat{\sigma}_z$	$\frac{\gamma}{2\hbar} e^{-\frac{\gamma}{\hbar}t} (\cosh(\omega t) + \frac{\gamma}{\hbar\omega} \sinh(\omega t))$
$\mathcal{E}_{AC1}$	0	$\hat{1}$	$\hat{L}^\dagger \hat{L} = \gamma\hat{1}$	$\hat{1}$ $\hat{\sigma}_z$	$-\frac{\gamma}{4\hbar} e^{-\frac{\gamma}{\hbar}t} (\cosh(\omega t) + \frac{\gamma}{\hbar\omega} \sinh(\omega t))$
$\mathcal{E}_{AC2}$	0	$\hat{L}^\dagger \hat{L} = \gamma\hat{1}$	$\hat{1}$	$\hat{1}$ $\hat{\sigma}_z$	$-\frac{\gamma}{4\hbar} e^{-\frac{\gamma}{\hbar}t} (\cosh(\omega t) + \frac{\gamma}{\hbar\omega} \sinh(\omega t))$

TABLE III. Analytic expressions contributing to  $\dot{C}(t)$  in Eq. (7). Results include equal contributions from the  $|0\rangle\langle 0|$  and  $|1\rangle\langle 1|$  components of  $\hat{\rho}_{eq}$  in each entry of the rightmost column. The operator  $\hat{\theta}_A$  is implemented by the combination of  $\hat{1}$  and  $\hat{\sigma}_z$ . For  $\mathcal{E}_D = \frac{1}{2}$ , we have no time evolution with  $\chi = 0$ ,  $\hat{N} = \hat{1}$ ,  $\hat{M} = \hat{1}$  and we input  $\hat{\theta}_B = \hat{1}$ . Further details of the expectation value terms are given in the SM.

respectively, from measurements of the control qubit  $q_c$ . Both circuits consume the three ancillary qubits ( $A_1-A_3$ ) to realise CW-Lindblad evolution this time evolution block is outlined by a dashed line in Fig. 9 but also present in Fig. 8. The single-qubit rotation angles are fixed by the Lindbladian parameters according to

$$\theta_z(t) = 2\sqrt{\frac{\gamma t}{N}}, \quad \theta_y(t) = 2\frac{\mu t}{N}, \quad (58)$$

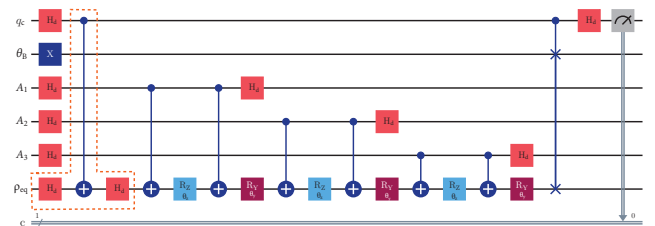


FIG. 8. Six-qubit circuit used to measure the correlation function  $\mathcal{E}_C(t)$ . Ancillary qubits  $A_1-A_3$  implement the CW-Lindblad time-evolution gate. All qubits start in  $|0\rangle$ . The gates inside the dashed box correspond to  $\hat{\theta}_A = \hat{\sigma}_z$  and are omitted for  $\hat{\theta}_A = \hat{1}$ . Single-qubit rotations in  $\hat{\rho}_{eq}$  channel are parametrised as  $\hat{R}_z(\theta_z)$  and  $\hat{R}_y(\theta_y)$ .

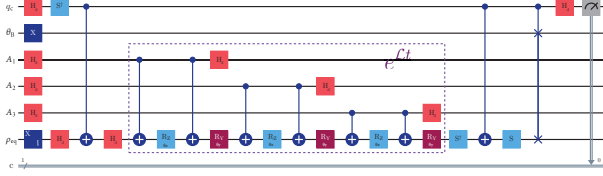


FIG. 9. Six-qubit Qiskit circuit used to evaluate the single expectation value  $\mathcal{E}_{\hat{H}_1}(t)$  that determines the transition rate  $\dot{C}(t)$ . The dashed box contains the CW-Lindblad evolution  $e^{\mathcal{L}_t}$  realised with the same three ancillas  $A_1-A_3$ . The bottom qubit is prepared in a maximally mixed state by applying either a  $\hat{\sigma}_x$  gate or the identity with equal probability.

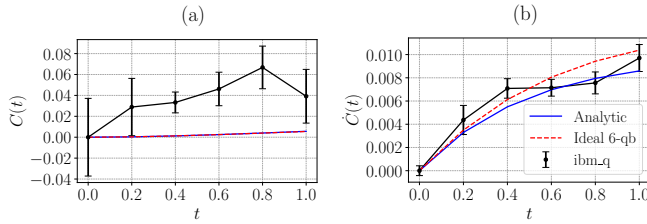


FIG. 10. Shifted experimental data: (a) correlation function  $C(t)$  and (b) rate  $\dot{C}(t)$  from the IBM Quantum run, compared with the analytic solution and the ideal six-qubit circuit. Parameters  $\mu = 0.1$ ,  $\gamma = 1$ ,  $\hbar = 1$ . Both traces are offset so that  $C(0) = 0$  and  $\dot{C}(0) = 0$ ; unshifted versions appear in the main text. Raw shot counts are listed in Tabs. V and VI.

where  $N$  is the number of ancilla iterations (three in the present experiment). The numerical values used are listed in Table IV.

$t$	0.0	0.2	0.4	0.6	0.8	1.0
$\theta_z$	0	$\frac{2}{\sqrt{15}}$	$\frac{2\sqrt{2}}{\sqrt{15}}$	$\frac{2\sqrt{3}}{\sqrt{15}}$	$\frac{4}{\sqrt{15}}$	$\frac{2\sqrt{5}}{\sqrt{15}}$
$\theta_y$	0	$\frac{1}{75}$	$\frac{2}{75}$	$\frac{3}{75}$	$\frac{4}{75}$	$\frac{5}{75}$

TABLE IV. The rotation gate parameters  $\theta_z$  and  $\theta_y$  are used in Figs. 8 and 9 for the various evolution times. The parameters are  $\gamma = 1$  and  $\mu = 0.1$  for our experiments.

For each run the control qubit is measured in the  $\hat{\sigma}_z$  basis at  $t = 0, 0.2, 0.4, 0.6, 0.8$ , and  $1$ . This yields ten batches of 20 000 shots for  $C(t)$  and five batches of 20 000 shots for  $\dot{C}(t)$ . The mean of each batch is reported together with its standard error; the complete raw data appear in Tables V and VI and are plotted in Fig. 4 of the main text.

To highlight device-induced offsets we also re-plot the data in Figs. 10(a) and 10(b) after shifting the experimental curves so that  $C(0) = 0$ . The shifted  $\dot{C}(t)$  traces closely follow the ideal six-qubit simulation (red dashed line), indicating that residual discrepancies at  $t = 0$  stem primarily from gate and measurement errors in the absence of time evolution. We further characterised statis-

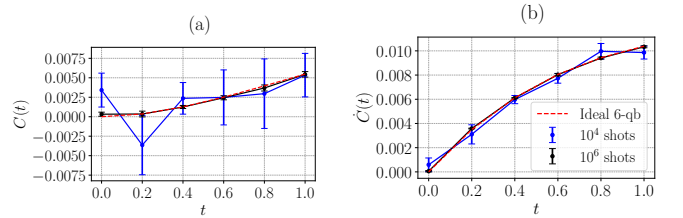


FIG. 11. Shot noise simulations performed on IBM Qiskit simulator: (a) correlation function  $C(t)$  (circuit in Fig. 8) and (b) rate  $\dot{C}(t)$  (circuit in Fig. 9), compared with a noiseless results. Parameters  $\mu = 0.1$ ,  $\gamma = 1$ ,  $\hbar = 1$ .

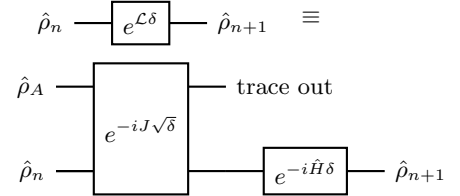


FIG. 12. Schrödinger picture time-evolution circuit [5]

tical noise by running the circuits in Figs. 8 and 9 on the Qiskit shot noise emulator. The results, shown in Fig. 11, demonstrate convergence toward the exact  $C(t)$  and  $\dot{C}(t)$  curves; notably, the  $\dot{C}(t)$  circuit converges significantly faster than the  $C(t)$  circuit, for reasons discussed in the main text.

### Cleve-Wang Lindblad evolution circuit

We recap the repeated interaction Lindblad simulation scheme described by Cleve and Wang in [5]. In their approach, time is discretised into  $N$  segments and an ancillary qudit with dimension  $d + 1$  is required where  $d$  is the number of Lindblad operators. The qudit state  $\hat{\rho}_A$  is initially prepared in

$$\hat{\rho}_A = |0_{d+1}\rangle \langle 0_{d+1}|. \quad (59)$$

Using qubit architectures, if  $d + 1$  is not a power of two, the qudit can be embedded into a qubit-based register with dimension  $2^n \geq d + 1$  for  $n$  qubits. The combined system undergoes the joint unitary evolution under the Hamiltonian-like operator

$$\hat{J} = \begin{pmatrix} 0 & \hat{L}_1^\dagger & \cdots & \hat{L}_d^\dagger \\ \hat{L}_1 & \ddots & & 0 \\ \vdots & & \ddots & \vdots \\ \hat{L}_d & 0 & \cdots & 0 \end{pmatrix}, \quad (60)$$

for the duration of  $\sqrt{\delta}$ , where  $\delta = \tau/N$ . After the ancillary qubit is traced out as shown in Fig. 12, the remaining reduced density matrix is evolved under  $\hat{H}$  for the time

step  $\delta$ . This process is repeated  $N$  times to simulate the approximate Lindblad dynamics with accuracy increasing with  $N$ .

For the first stage, in block matrix notation, the total input state is given by  $|0_{d+1}\rangle\langle 0_{d+1}| \otimes \hat{\rho}$ . The joint unitary evolution is given by

$$\begin{aligned} e^{-i\hat{J}\sqrt{\delta}} (|0_{d+1}\rangle\langle 0_{d+1}| \otimes \hat{\rho}) e^{i\hat{J}\sqrt{\delta}} \approx \\ |0_{d+1}\rangle\langle 0_{d+1}| \otimes \hat{\rho} - i \left[ \hat{J}, (|0_{d+1}\rangle\langle 0_{d+1}| \otimes \hat{\rho}) \right] \sqrt{\delta} \\ + \left( \hat{J} (|0_{d+1}\rangle\langle 0_{d+1}| \otimes \hat{\rho}) \hat{J} - \frac{1}{2} \hat{J}^2 (|0_{d+1}\rangle\langle 0_{d+1}| \otimes \hat{\rho}) \right) \\ - \frac{1}{2} (|0_{d+1}\rangle\langle 0_{d+1}| \otimes \hat{\rho}) \hat{J}^2 \right) \delta + O(\delta^{3/2}). \quad (61) \end{aligned}$$

The only non-zero entries of the commutator term are off-diagonal in the tensor product representation. The reduced density matrix after tracing out the ancillary channel can be evolved under the Hamiltonian  $\hat{H}$ , giving

$$\begin{aligned} \hat{\rho} \rightarrow \hat{\rho} - i[\hat{H}, \hat{\rho}] \delta \\ + \sum_{k=1}^d \left( \hat{L}_k \hat{\rho} \hat{L}_k^\dagger - \frac{1}{2} \hat{L}_k^\dagger \hat{L}_k \hat{\rho} - \frac{1}{2} \hat{\rho} \hat{L}_k^\dagger \hat{L}_k \right) \delta + O(\delta^{3/2}). \quad (62) \end{aligned}$$

Taking this output density matrix and feeding it back into the Lindblad evolution circuit for  $N$  iterations, it approximately becomes the time-evolved density matrix  $\hat{\rho}(\tau)$ .

### Quantum Brownian motion in a 1D double well

Caldeira and Leggett derived the master equation that governs the evolution of the reduced density operators of a quantum particle coupled to a bath of thermal oscillators [7]. This Caldeira-Leggett (CL) master equation is expressed with  $\hat{H}_{CL} = \hat{P}^2/(2m) + V(\hat{X})$

$$\begin{aligned} \frac{d}{dt} \hat{\rho}_s &= -\frac{i}{\hbar} [\hat{H}_{CL}, \hat{\rho}_s] - \frac{i\gamma}{\hbar} [\hat{X}, \{\hat{P}, \hat{\rho}_s\}] \\ &- \frac{2m\gamma k_B T}{\hbar^2} [\hat{X}, [\hat{X}, \hat{\rho}_s]], \quad (63) \end{aligned}$$

where  $\hat{X}$  and  $\hat{P}$  are the position and momentum operators of the quantum particle.

The above CL dynamics does not unfortunately maintain the positivity of the density matrix, especially at reduced temperatures. Addressing this limitation, a modification in Ref. [8] introduces a new term such as

$$-\frac{\gamma}{8mk_B T} [\hat{P}, [\hat{P}, \hat{\rho}_s]], \quad (64)$$

which becomes insignificant at elevated temperatures. This ensures the positivity of the density matrix and

allows the dynamics to be recast in the positivity preserving Lindblad form [9, 10]

$$\frac{d}{dt} \hat{\rho}_S = -\frac{i}{\hbar} [\hat{H}, \hat{\rho}_S] + \frac{1}{\hbar} \left( \hat{L} \hat{\rho}_S \hat{L}^\dagger - \frac{1}{2} \{\hat{\rho}_S, \hat{L}^\dagger \hat{L}\} \right), \quad (65)$$

with  $\lambda_T = \sqrt{\hbar/4mk_B T}$ . Its Hamiltonian and Lindblad operators are

$$\hat{H} = \frac{\hat{P}^2}{2m} + \hat{V}(\hat{X}) + \frac{\gamma}{2} (\hat{X} \hat{P} + \hat{P} \hat{X}), \quad (66)$$

$$\hat{L} = \sqrt{\gamma} \left( \lambda_T^{-1} \hat{X} + i \lambda_T \hat{P} \right). \quad (67)$$

where  $\hat{X}$  and  $\hat{P}$  are the position and momentum operators.

### UNITARY IMPLEMENTATION OF POSITION SPACE

For the Caldeira Leggett discrete position representation and the wave function with  $n$  qubits is given over the coordinate interval  $x \in [0, 1 - 2^{-n}]$  using QuTiP [11]. The position operator is defined as

$$\hat{X} = \sum_{k=0}^{2^n-1} x_k |x_k\rangle\langle x_k|, \quad (68)$$

This position space grid induces a momentum grid that satisfies the discrete uncertainty relation, known as the error-disturbance uncertainty relation [12],  $\delta x \delta p = 2\pi\hbar/2^n$  implying momentum spacing  $\delta p = 2\pi\hbar$ . Then, the momentum eigenstates have eigenvalues  $p_j = (-2^{n-1} + j)\delta p$  for  $j = 0, 1, \dots, 2^n - 1$  and the momentum operator is defined as

$$\hat{P} = \sum_{j=0}^{2^n-1} p_j |p_j\rangle\langle p_j| = \sum_{j,k,l=0}^{2^n-1} p_j \tilde{U}_{jk} |x_k\rangle\langle x_l| \tilde{U}_{lj}^\dagger, \quad (69)$$

where the unitary matrix  $\tilde{U}$  is related to the quantum Fourier transform:

$$\tilde{U}_{jk} = \frac{1}{\sqrt{2^n}} \exp \left( \frac{i}{\hbar} x_j p_k \right). \quad (70)$$

We adopt the  $n$ -qubit grid representation  $x \in [0, 1 - 2^{-n}]$  used in QuTiP [11]. The position operator is

$$\hat{X} = \sum_{k=0}^{2^n-1} x_k |x_k\rangle\langle x_k|, \quad (71)$$

and the associated momentum spacing  $\delta p = 2\pi\hbar$  satisfies the discrete uncertainty relation

$$\delta x \delta p = \frac{2\pi\hbar}{2^n}, \quad \delta x = 2^{-n}, \quad (72)$$

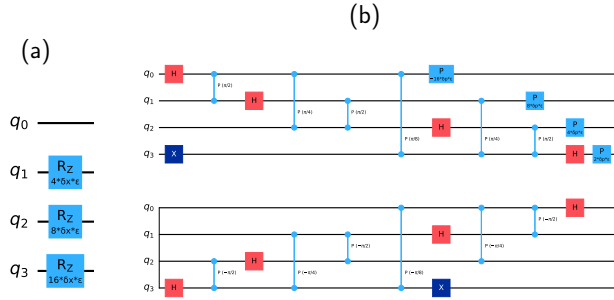


FIG. 13. Four-qubit Qiskit implementation of  $U(\hat{X}, \epsilon)$  (a) and  $U(\hat{P}, \epsilon)$  (b). Extra Not gates on the most significant bit in (b), map the domain from  $[0, 1]$  to  $[-\frac{1}{2}, \frac{1}{2}]$  and back.

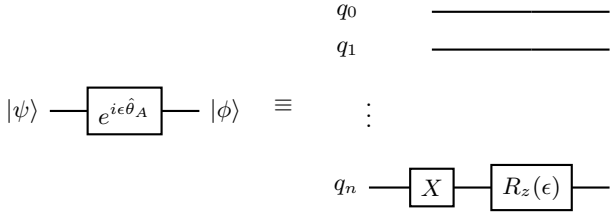


FIG. 14. Unitary used in  $\hat{\theta}_A$  approximation. The Not and  $R_z(\epsilon)$  are applied to the most significant qubit affecting only the smallest  $2^{n-1}$  gridpoints

with  $p_j = (-2^{n-1} + j)\delta p$  ( $j = 0, \dots, 2^n - 1$ ) the momentum operator reads

$$\hat{P} = \sum_{j=0}^{2^n-1} p_j |p_j\rangle \langle p_j| = \sum_{j,k,l=0}^{2^n-1} p_j U_{jk} |x_k\rangle \langle x_l| U_{lj}^\dagger, \quad (73)$$

where the quantum-Fourier-transform matrix is

$$U_{jk} = \frac{1}{\sqrt{2^n}} \exp(i x_j p_k / \hbar). \quad (74)$$

Any Hermitian operator  $\hat{O} \in \{\hat{\theta}_A, \hat{X}, \hat{P}\}$  is approximated by a small-angle unitary

$$\hat{O}_\epsilon \simeq \frac{U(\hat{O}, \epsilon) - U(\hat{O}, -\epsilon)}{2i\epsilon} \quad \text{with} \quad U(\hat{O}, \epsilon) = \exp(i\epsilon \hat{O}). \quad (75)$$

In Figs. 13 and 14 we show basic unitary implementations of  $U(\hat{X}, \epsilon)$ ,  $U(\hat{P}, \epsilon)$  and  $U(\hat{\theta}_{A,\epsilon})$ . We use  $U(\hat{X}, \epsilon)$  and  $U(\hat{P}, \epsilon)$  as building blocks to generate approximate unitary decompositions of arbitrary powers and combinations of  $\hat{X}$  and  $\hat{P}$ . For small  $\epsilon$ , a sequence of finite difference identities provides the required operator recon-

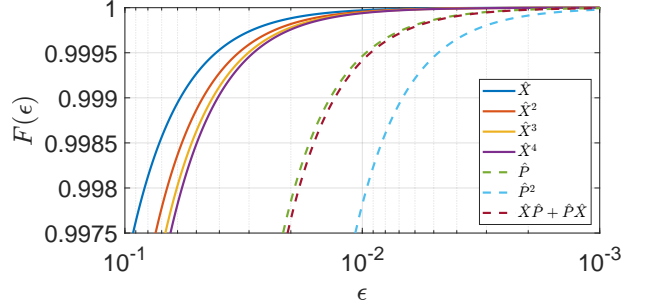


FIG. 15. Gate fidelities of the unitary approximations as a function of  $\epsilon$  for simulations performed in a truncated five-qubit Hilbert space ( $d = 2^5 = 32$ ) representing a uniform grid over the interval  $[0, 1]$ .

structions given explicitly by

$$\hat{X} \approx \frac{U(\hat{X}, \epsilon) - U(\hat{X}, -\epsilon)}{2i\epsilon}, \quad (76)$$

$$\hat{P} \approx \frac{U(\hat{P}, \epsilon) - U(\hat{P}, -\epsilon)}{2i\epsilon}, \quad (77)$$

$$\hat{X}^2 \approx -\frac{U(\hat{X}, \epsilon) + U(\hat{X}, -\epsilon) - 2\hat{1}}{\epsilon^2}, \quad (78)$$

$$\hat{P}^2 \approx -\frac{U(\hat{P}, \epsilon) + U(\hat{P}, -\epsilon) - 2\hat{1}}{\epsilon^2}, \quad (79)$$

$$\begin{aligned} \hat{X}^3 &\approx -\frac{i}{2\epsilon^3} (U(\hat{X}, \epsilon)^2 - U(\hat{X}, -\epsilon)^2 \\ &\quad - 2(U(\hat{X}, \epsilon) - U(\hat{X}, -\epsilon))), \end{aligned} \quad (80)$$

$$\begin{aligned} \hat{X}^4 &\approx \frac{1}{\epsilon^4} (U(\hat{X}, -\epsilon)^2 - 4U(\hat{X}, -\epsilon) + 6\hat{1} \\ &\quad - 4U(\hat{X}, \epsilon) + U(\hat{X}, \epsilon)^2). \end{aligned} \quad (81)$$

For the mixed second-order symmetrized product we use

$$\begin{aligned} \hat{X}\hat{P} + \hat{P}\hat{X} &\approx -\frac{1}{4\epsilon^2} \left( U(\hat{X}, \epsilon)U(\hat{P}, \epsilon) + U(\hat{P}, \epsilon)U(\hat{X}, \epsilon) \right. \\ &\quad - U(\hat{X}, \epsilon)U(\hat{P}, -\epsilon) - U(\hat{P}, -\epsilon)U(\hat{X}, \epsilon) \\ &\quad - U(\hat{X}, -\epsilon)U(\hat{P}, \epsilon) - U(\hat{P}, \epsilon)U(\hat{X}, -\epsilon) \\ &\quad \left. + U(\hat{X}, -\epsilon)U(\hat{P}, -\epsilon) + U(\hat{P}, -\epsilon)U(\hat{X}, -\epsilon) \right). \end{aligned} \quad (82)$$

Here  $U(\hat{X}, \epsilon)^2 \equiv U(\hat{X}, \epsilon)U(\hat{X}, \epsilon) = U(\hat{X}, 2\epsilon)$  (and similarly for  $\hat{P}$ ).

From these relations we see that all requisite powers of  $\hat{X}$  and  $\hat{P}$  may be assembled as linear combinations of the primitive circuits  $\{\hat{1}, U(\hat{X}, \epsilon), U(\hat{P}, \epsilon), U(\hat{X}, 2\epsilon), U(\hat{P}, 2\epsilon), U(\hat{X}, \epsilon)U(\hat{P}, \epsilon), U(\hat{P}, \epsilon)U(\hat{X}, \epsilon)\}$ . In Fig. 15 we plot the operator “gate fidelities”

$$F(\epsilon) \equiv 1 - \frac{1}{2} \|\hat{O}_\epsilon - \hat{O}\|_1, \quad (83)$$

where  $\|X\|_1$  is the sum of the singular values of  $X$  [13]. Here  $\hat{O}_\epsilon$  denotes the operator obtained from our

finite-displacement unitary reconstruction at step size  $\epsilon$ , and  $\hat{\mathcal{O}}$  is the corresponding exact Hermitian target (e.g.,  $\hat{X}$ ,  $\hat{X}^2$ ,  $\hat{P}$ ,  $\{\hat{X}, \hat{P}\}$ , etc.). The curves are shown as functions of  $\epsilon$  for simulations performed in a truncated five-qubit Hilbert space ( $d = 2^5 = 32$ ) representing a uniform grid over the interval  $[0, 1]$ . Across the explored range  $10^{-1} \geq \epsilon \geq 10^{-3}$  we observe high fidelities.

### Controlled-SWAP gate for mixed states

In this section we define a controlled-SWAP (C-SWAP) for two density operators on  $\hat{A} \otimes \hat{B}$ . Suppose we have the following two density operators such as

$$\hat{A} = \sum_{ij} a_{ij} |i\rangle\langle j|, \quad \text{and} \quad \hat{B} = \sum_{kl} b_{kl} |k\rangle\langle l|. \quad (84)$$

The control qubit can be expressed in four components such as  $|0\rangle\langle 0|$ ,  $|0\rangle\langle 1|$ ,  $|1\rangle\langle 0|$ , and  $|1\rangle\langle 1|$ . The first and last components, when combined with the C-SWAP circuit, result in  $|0\rangle\langle 0| \otimes \hat{A} \otimes \hat{B}$  and  $|1\rangle\langle 1| \otimes \hat{B} \otimes \hat{A}$ . If we consider the control input  $|1\rangle\langle 0|$ , the outcome is given by

$$\begin{aligned} \mathbf{C}_{\text{SWAP}} & \left( |1\rangle\langle 0| \otimes \left( \sum_{ijkl} a_{ij} b_{kl} |i\rangle\langle j| \otimes |k\rangle\langle l| \right) \right) \\ & = |1\rangle\langle 0| \otimes \left( \sum_{ijkl} a_{ij} b_{kl} |k\rangle\langle j| \otimes |i\rangle\langle l| \right). \end{aligned} \quad (85)$$

Similarly, for the control input  $|0\rangle\langle 1|$ , we have

$$\begin{aligned} \mathbf{C}_{\text{SWAP}} & \left( |0\rangle\langle 1| \otimes \left( \sum_{ijkl} a_{ij} b_{kl} |i\rangle\langle j| \otimes |k\rangle\langle l| \right) \right) \\ & = |0\rangle\langle 1| \otimes \left( \sum_{ijkl} a_{ij} b_{kl} |i\rangle\langle l| \otimes |k\rangle\langle j| \right). \end{aligned} \quad (86)$$

These states are entangled and cannot be simply expressed in terms of the original operators  $\hat{A}$  and  $\hat{B}$ . However, if we take the partial trace over the  $\hat{A}$  and  $\hat{B}$  channels, the resulting states are

$$\text{Tr}(\hat{A}\hat{B}) |1\rangle\langle 0| \quad \text{and} \quad \text{Tr}(\hat{A}\hat{B}) |0\rangle\langle 1| \quad (87)$$

respectively for each choice of control qubit. In this way, the C-SWAP operation allows the multiplication of the two channels. To allow us to keep track of swapped states without expanding into a basis, we define a new notation for the state as referenced in Eq. (85) as follows

$$\sum_{ijkl} a_{ij} b_{kl} |k\rangle\langle j| \otimes |i\rangle\langle l| = \hat{A} \xleftrightarrow{k} \hat{B}, \quad (88)$$

where the “k” signifies that we are swapping the ket parts of the projectors. Similarly, for the state referenced in Eq. (86), we have

$$\sum_{ijkl} a_{ij} b_{kl} |i\rangle\langle l| \otimes |k\rangle\langle j| = \hat{A} \xleftrightarrow{b} \hat{B} \quad (89)$$

where “b” denotes a bra part swap. After the C-SWAP gate, we have the output states

$$|0\rangle\langle 0| \otimes \hat{A} \otimes \hat{B} \otimes \hat{C} \rightarrow |0\rangle\langle 0| \otimes \hat{A} \otimes \hat{C} \otimes \hat{B}, \quad (90)$$

$$|1\rangle\langle 1| \otimes \hat{A} \otimes \hat{B} \otimes \hat{C} \rightarrow |1\rangle\langle 1| \otimes \hat{B} \otimes \hat{A} \otimes \hat{C}, \quad (91)$$

$$|0\rangle\langle 1| \otimes \hat{A} \otimes \hat{B} \otimes \hat{C} \rightarrow |0\rangle\langle 1| \otimes \left( \hat{A} \xleftrightarrow{b1} \hat{B} \right) \xleftrightarrow{b2} \hat{C}, \quad (92)$$

$$|1\rangle\langle 0| \otimes \hat{A} \otimes \hat{B} \otimes \hat{C} \rightarrow |1\rangle\langle 0| \otimes \left( \hat{A} \xleftrightarrow{k1} \hat{B} \right) \xleftrightarrow{k2} \hat{C}. \quad (93)$$

Taking the trace-out of the state of  $|0\rangle\langle 1|$ , we have

$$\text{Tr} \left( \sum_{ijklmn} a_{ij} b_{kl} c_{mn} |i\rangle\langle l| \otimes |m\rangle\langle j| \otimes |k\rangle\langle n| \right) = \text{Tr}(\hat{B}\hat{A}\hat{C}). \quad (94)$$

Similarly, the trace-out of the state of  $|1\rangle\langle 0|$  gives

$$\text{Tr} \left( \sum_{ijklmn} a_{ij} b_{kl} c_{mn} |k\rangle\langle j| \otimes |i\rangle\langle n| \otimes |m\rangle\langle l| \right) = \text{Tr}(\hat{A}\hat{B}\hat{C}). \quad (95)$$

### IBM QUANTUM RAW DATA

Tables V and VI show the raw data from the correlation function and the rate simulations of the metastable spin- $\frac{1}{2}$  system, using the *ibm\_brisbane* quantum processor.

- 
- [1] D. Chandler, *Introduction to Modern Statistical Mechanics* (Oxford University Press, Oxford, 1987).
  - [2] L. Onsager, Phys. Rev. **38**, 2265 (1931).
  - [3] A. M. Berezhkovskii and A. Szabo, J. Phys. Chem. B **127**, 5084 (2023).
  - [4] I. R. Craig and D. E. Manolopoulos, J. Chem. Phys. **121**, 3368 (2004).
  - [5] R. Cleve and C. Wang, *the 44th International Colloquium on Automata, Languages, and Programming (ICALP 2017)* (Schloss Dagstuhl–Leibniz-Zentrum für Informatik, 2017) p. 17.
  - [6] J. Joo and T. P. Spiller, New J. Phys. **25**, 083041 (2023).
  - [7] A. O. Caldeira and A. J. Leggett, Phys. A: Stat. Mech. Appl. **121**, 587 (1983).

<b>Attempt</b>	$t_0 = 0.0$			$t_0 = 0.2$			$t_0 = 0.4$		
	$\hat{\theta}_A = \hat{1}$	$\hat{\theta}_A = \hat{\sigma}_z$	$\mathcal{E}_C$	$\hat{\theta}_A = \hat{1}$	$\hat{\theta}_A = \hat{\sigma}_z$	$\mathcal{E}_C$	$\hat{\theta}_A = \hat{1}$	$\hat{\theta}_A = \hat{\sigma}_z$	$\mathcal{E}_C$
1	5266	5222	0.0488	6199	5094	0.1293	5102	5424	0.0526
2	6243	4605	0.0848	5727	4944	0.0671	5103	5307	0.0410
3	6560	4984	0.1544	5008	5110	0.0118	4325	5928	0.0253
4	2267	5065	-0.2668	5028	5841	0.0869	5296	5275	0.0571
5	5198	5001	0.0199	3140	4978	-0.1882	5094	5555	0.0649
6	5533	3884	-0.0583	5590	4512	0.0102	4570	5193	-0.0237
7	5121	5248	0.0369	5470	4953	0.0423	5537	5257	0.0794
8	5608	5171	0.0779	5050	5833	0.0883	5547	4884	0.0431
9	5320	5229	0.0549	5299	5257	0.0556	5251	5406	0.0657
10	3964	5268	-0.0768	5276	5335	0.0611	5056	4973	0.0029
<b>Mean</b>	<b>0.00757</b>			<b>0.03644</b>			<b>0.04083</b>		
<b>SEM</b>	<b>0.03714</b>			<b>0.02740</b>			<b>0.00997</b>		
<b>Attempt</b>	$t_0 = 0.6$			$t_0 = 0.8$			$t_0 = 1.0$		
	$\hat{\theta}_A = \hat{1}$	$\hat{\theta}_A = \hat{\sigma}_z$	$\mathcal{E}_C$	$\hat{\theta}_A = \hat{1}$	$\hat{\theta}_A = \hat{\sigma}_z$	$\mathcal{E}_C$	$\hat{\theta}_A = \hat{1}$	$\hat{\theta}_A = \hat{\sigma}_z$	$\mathcal{E}_C$
1	4937	4925	-0.0138	5207	6216	0.1423	5207	5840	0.1047
2	5133	5671	0.0804	5483	5104	0.0587	6401	5823	0.2224
3	5317	5071	0.0388	4426	5008	-0.0566	5868	5035	0.0903
4	4293	5992	0.0285	5972	5258	0.1230	4350	5438	-0.0212
5	5615	5714	0.1329	4899	6220	0.1119	5276	5110	0.0386
6	6022	5133	0.1155	5698	5682	0.1380	5086	5102	0.0188
7	5775	4378	0.0153	5066	4859	-0.0075	4901	4494	-0.0605
8	4943	4972	-0.0085	5379	5331	0.0710	5174	5347	0.0521
9	5740	4813	0.0553	6248	4765	0.1013	5142	5405	0.0547
10	5493	5437	0.0930	5272	5341	0.0613	4392	5285	-0.0323
<b>Mean</b>	<b>0.05374</b>			<b>0.07434</b>			<b>0.04676</b>		
<b>SEM</b>	<b>0.01602</b>			<b>0.02040</b>			<b>0.02569</b>		

TABLE V. IBMQ data for  $C(t)$  with  $t = \{0, 0.2, 0.4, 0.6, 0.8, 1.0\}$  and  $\hat{\rho}_{eq} = |0\rangle\langle 0|$ . Ten data sets were collected with the circuits in Fig. 8 (20000 shots each). Counts in the  $\hat{\theta}_A$  columns correspond to measuring  $|0\rangle$  on the control qubit; contributions from  $\hat{\rho}_{eq} = |1\rangle\langle 1|$  cancel.

<b>Attempt</b>	$t_0 = 0.0$			$t_0 = 0.2$			$t_0 = 0.4$		
	$\hat{\rho}_{eq} =  0\rangle\langle 0 $	$\hat{\rho}_{eq} =  1\rangle\langle 1 $	$\mathcal{E}_{H1}$	$\hat{\rho}_{eq} =  0\rangle\langle 0 $	$\hat{\rho}_{eq} =  1\rangle\langle 1 $	$\mathcal{E}_{H1}$	$\hat{\rho}_{eq} =  0\rangle\langle 0 $	$\hat{\rho}_{eq} =  1\rangle\langle 1 $	$\mathcal{E}_{H1}$
1	4816	5087	-0.0009700	5218	4787	0.00005000	5339	4834	0.001730
2	4873	5117	-0.0001000	5335	4980	0.0003150	5435	4929	0.003640
3	4840	5050	-0.001100	5283	4809	0.0009200	5368	4834	0.002020
4	4874	5083	-0.0004300	4868	5166	0.0003400	5404	4866	0.002700
5	4863	5018	-0.001190	5283	4984	0.002670	5351	5032	0.003830
<b>Mean</b>	<b>-0.0007580</b>			<b>0.001426</b>			<b>0.002784</b>		
<b>SEM</b>	<b>0.0002108</b>			<b>0.0006264</b>			<b>0.0004200</b>		
<b>Attempt</b>	$t_0 = 0.6$			$t_0 = 0.8$			$t_0 = 1.0$		
	$\hat{\rho}_{eq} =  0\rangle\langle 0 $	$\hat{\rho}_{eq} =  1\rangle\langle 1 $	$\mathcal{E}_{H1}$	$\hat{\rho}_{eq} =  0\rangle\langle 0 $	$\hat{\rho}_{eq} =  1\rangle\langle 1 $	$\mathcal{E}_{H1}$	$\hat{\rho}_{eq} =  0\rangle\langle 0 $	$\hat{\rho}_{eq} =  1\rangle\langle 1 $	$\mathcal{E}_{H1}$
1	5316	4843	0.001590	5196	5020	0.002160	5573	4892	0.004650
2	5299	5084	0.003830	5374	4941	0.003150	5413	4998	0.004110
3	5422	4886	0.003080	5327	4962	0.002890	5420	5004	0.004240
4	5309	4966	0.002750	5299	4918	0.002170	5314	4884	0.001980
5	5332	4950	0.002820	5512	4962	0.004740	5157	5392	0.005490
<b>Mean</b>	<b>0.002814</b>			<b>0.003022</b>			<b>0.004094</b>		
<b>SEM</b>	<b>0.0003609</b>			<b>0.0004719</b>			<b>0.0005809</b>		

TABLE VI. IBMQ data for  $\dot{C}(t)$ : For each value of  $t = \{0, 0.2, 0.4, 0.6, 0.8, 1\}$  and  $\hat{\rho}_{eq} = |0\rangle\langle 0|$  or  $\hat{\rho}_{eq} = |1\rangle\langle 1|$ , the five sets of the circuits in Fig. 9 were performed and each set is made with 10,000 shots. The values in the  $\hat{\rho}_{eq} = |0\rangle\langle 0|$  and  $\hat{\rho}_{eq} = |1\rangle\langle 1|$  columns represent the counts with measurement outcome  $|0\rangle$  in the control qubit. Each pair in these two columns is used to calculate the expectation values  $\mathcal{E}_{H1}$ .

- [8] I. J. David, I. Sinayskiy, and F. Petruccione, *Quanta* **12**, 131 (2023).
- [9] V. Gorini, A. Kossakowski, and E. C. G. Sudarshan, *J. Math. Phys.* **17**, 821 (1976).
- [10] G. Lindblad, *Commun. Math. Phys.* **48**, 119 (1976).
- [11] J. R. Johansson, P. D. Nation, and F. Nori, *Comput. Phys. Commun.* **183**, 1760 (2012).
- [12] O. Kabernik, *Phys. Rev. A* **104**, 052206 (2021).
- [13] M. A. Nielsen and I. L. Chuang, *Quantum Computation and Quantum Information* (Cambridge University Press, 2010).